Tracer model-based quantitative separation of precipitation and permafrost waters used for evapotranspiration in a boreal forest

Hotaek Park[1,2,*], Masahiro Tanoue[3], Kimpei Ichiyanagi[4], Go Iwahana[5], and Tetsuya Hiyama[2]

[1]Institute of Arctic Climate and Environment Research, JAMSTEC, Yokosuka, Japan. [2]Institute for Space-Earth Environmental Research, Nagoya University, Nagoya, Japan. [3]Center for Global Environmental Research, National Institute for Environmental Studies, Ibaraki, Japan. [4]Faculty of Advanced Science and Technology, Kumamoto University, Kumamoto, Japan. [5]International Arctic Research Center, University of Alaska, Fairbanks, USA.

*Corresponding author: Hotaek Park (park@jamstec.go.jp)

Key Points

- Tracer model separates contributions of precipitation- and permafrost-originated waters to evapotranspiration in deciduous boreal forest

- Rainfall is a primary source for seasonal and interannual variability of evapotranspiration

- The isotope process coupled to the tracer model supports the soundness of the partitioned quantification

Abstract

Arctic precipitation (P_G) that occurs as rainfall (P_r) or snowfall (P_s) depending on the prevailing climatic conditions results in seasonally specific hydrological events. Climate change can affect the P_G- and permafrost-originated water (P_i) regimes, resulting in change to ecohydrological processes. However, the relative influences of source waters (i.e., P_r, P_s, and P_i) on terrestrial hydrological processes have not yet been fully established. Here, we report the development and implementation of a numerical water tracer model designed to quantify changes in the storages and fluxes of the source waters and the hydrogen and oxygen isotopic tracers associated with hydrometeorological events. The presented tracer model was used to illustrate the spatiotemporal variability of the tracers in the surface–subsurface system of a deciduous needleleaf boreal forest, and to separate the contribution rates of the tracer waters to evapotranspiration (*ET*). Although P_s accounted for 14%–40% of *ET* and the subcomponents, the contribution rates to soil evaporation and transpiration were significant only during the spring season. The major source water for soil moisture was P_r, which accounted for 80.1% of *ET* and showed an increasing trend. Additionally, P_r also accounted for 85.7% of transpiration. Under the present conditions of warming permafrost, P_i demonstrated negligibly low impact on *ET*. The tracer model was shown capable of quantifying the contribution rates of tracer waters to *ET*, highlighting the advantages of the tracer model for similar quantitative separation regarding future climate change.

Plain Language Summary

Although snowfall and rainfall are seasonally different processes, their influence on hydrological processes (i.e., evapotranspiration and river discharge) occurs mainly during the growing season. Quantification of their contributions to hydrological processes is an ongoing scientific problem in Arctic hydrology. Thus, we developed a tracer model, which includes isotopic processes, to separate the contributions of snowfall, rainfall, and permafrost-originated water to evapotranspiration and applied it to a boreal forest. The model simulation suggested that summer rainfall has greatest impact on evapotranspiration, while water from snowfall is strongly implicated in springtime evaporation. Permafrost-originated water is not connected directly to evapotranspiration at this study site. However, the future warming climate could potentially increase the role of permafrost-related water in ecohydrological processes. Thus, the presented water tracer model could potentially provide quantitative assessment of the changes in the physics of water dynamics caused by climate change.

1. Introduction

The effects of recent climate change are more significant in cold regions relative to warm regions. Observational records from Arctic meteorological stations document the evident trend of warming of surface air temperature (T_a) over recent decades (Bekryaev et al., 2010). This warming of T_a has resulted in various changes in cryospheric, hydrological, and ecological processes such as permafrost degradation and deepening of the active layer thickness (ALT) (Park et al., 2016), earlier onset of snowmelt (Kim et al., 2015), and higher vegetation productivity with the development of understory vegetation (Ohta et al., 2014). The enhanced ecohydrological connectivity between soil wetting and canopy greening induced by climate change likely increases water loss to the atmosphere via evapotranspiration (*ET*). In situ observations (Ohta et al., 2014) and model simulations (Zhang et al., 2010) indicate an increased trend of *ET*, which has been particularly significant during the recent two decades when T_a has increased markedly (Bekryaev et al., 2010). Moreover, resultant effects of climate change such as the changed landscape structure and lengthened growing season can alter the *ET* ratios apportioned to transpiration (E_t), canopy interception (E_i), and evaporation from soil (E_s) and water surfaces. However, the changes to *ET* and the subcomponents in warming Arctic regions have been poorly understood.

Earlier onset of snowmelt and subsequent thawing of frozen soil (Kim et al., 2015) can lead to soil wetting and likely advanced initiation of both E_s and E_t. Moreover, the longer growing season associated with climate change increases the proportion of rainfall in total annual precipitation (P_G) (Bintanja and Andry, 2017), which increases the amount of water input into the soil surface. On entering the soil column, this water mixes with resident older water and/or permafrost-originated water

(P_i). The mixing, mobilization, and fluxes associated with this water are likely further enhanced under the situation of a deepening ALT, consequentially altering the fractions of snow water (P_s), rainwater (P_r), and P_i comprising the soil moisture. As the hydrological dynamics of these three source waters are determined by seasonally characteristic events, changes in soil moisture influenced by the source waters can affect water budget components, particularly the processes of E_s and E_t that use soil moisture. Indeed, an isotope observational study identified an isotopic signal indicating plants extract permafrost-originated water under conditions of low soil moisture (Sugimoto et al., 2003). Other studies have presented isotopic evidence showing that plants do not use soil water participating in groundwater recharge and streamflow (Evaristo et al., 2015; Brooks et al., 2010; Goldsmith et al., 2012).

Stable water isotopes have been used successfully to understand how water is stored and released in the process of runoff generation, based on the isotopic damping signals from P_G to streamflow (McGuire et al., 2005; Jasechko et al., 2016; Lachniet et al., 2016; Welp et al., 2005). Stable water isotopes have also been used to investigate transpiration–evaporation partitioning, which led to an estimate that transpiration represents 60%–90% of terrestrial *ET* (Gibson and Edwards, 2002; Good et al., 2015; Jasechko et al., 2013). Good et al. (2015) quantified that 65% of evaporation originates from soils and not surface waters. The capabilities of using isotopes in related research have been amplified further through incorporation of an isotopic module in various land surface models (LSMs) (e.g., Aleinov and Schmidt, 2006; Fischer, 2006; Yoshimura et al., 2006; Sturm et al., 2010; Risi et al., 2016; Hu et al., 2018). Isotope-coupled LSMs have been used to simulate the changes in isotopic composition associated with the storage, flux, and residence time of water flow in the surface–subsurface system.

However, the transformations of isotopic compositions might hinder the use of isotope-enabled LSMs for tracking water of individual events. To overcome the limitations of existing LSMs, Hu et al. (2018) developed a new numerical tracer model that tags the water of a P_G event and tracks the pathways of water movement until leaving the system as either *ET* or runoff. Up to now, however, observations and isotope-enabled tracer models have provided little quantitative information on the fractions of P_r, P_s, and P_i comprising soil moisture or on their contribution rates to hydrological processes, including long-term trends under the effects of climate change.

Here, we present a water tracer model to delineate the movements of P_r, P_s, and P_i in permafrost regions and to quantify their contributions to hydrological processes, including changes in the concentration of hydrogen and oxygen isotopes. In the modeling, the tracer model considers five tracer components as analytical targets and quantifies the changes of the tracer concentrations occurring via the storage and fluxes associated with water movements. The main objective of this study was to quantify the relative contribution rates of P_r, P_s, and P_i source waters to hydrological processes, particularly *ET* processes, in a boreal larch forest during 1980–2016. Specifically, this study examined the seasonal and interannual variability of the three tracers to explore their responses to hydrometeorological events. Three sensitivity experiments that used different root profile schemes were also conducted to assess the influence of root profiles on E_t, soil moisture, and stable water isotopes.

2. Methods

2.1 General model description

This study used the coupled hydrological and biogeochemical model (CHANGE; Park et al., 2011, 2018), which is a process-based LSM that comprises a land surface module, biogeochemical dynamics module, and vegetation dynamics module. Thus, the model calculates momentum, heat, water, carbon fluxes, and plant physiology in the atmosphere–vegetation–snow–soil system. CHANGE provides insight into the interactions and feedbacks between ecosystem processes and the ambient atmosphere. The model simulates the accumulation and melt of the snowpack on the land surface, and the meltwater is partitioned consistently into surface runoff and soil infiltration, even during precipitation events. The excess of vertically infiltrated water at either the permafrost table or the bottom soil boundary layer is added to the subsurface runoff. Permafrost is an important component linked to hydrothermal processes in the subarctic terrestrial region. The model resolves soil heat and water flow, and it represents the hydrothermal dynamics of permafrost explicitly through consideration of the freezing/thawing phase transitions in a 1D soil column of 72.4-m depth. Water flow in the permafrost soil layers is represented by parameterization of ice blocking that limits liquid flow. The effects of soil organic carbon (SOC) on the hydraulic and thermal dynamics of the soil are represented through parameterization of the vertical distribution of SOC in the model.

The ice content in frozen soil layers reduces the effective porosity and thus decreases soil water availability to plant roots, which consequently increases the probability of water stress. In CHANGE, the soil moisture limitation that represents the stressful conditions associated with drying and/or freezing (i.e., $<-2°C$) is parameterized (value: 0–1). The parameter is coupled to the maximum rate of carboxylation, which varies as a function of leaf temperature, soil moisture, day length,

and nitrogen availability (Oleson et al., 2010). Initiation of leaf onset is controlled by a critical degree-day summation of soil temperature at 4 cm depth (White et al., 1997). These parameterizations represent the impact of the thermal states of permafrost on photosynthesis and stomatal conductance, as well as the overall behavior of plant phenology. CHANGE simulates biogeochemical processes across multiple biomes, including the carbon and nitrogen cycling associated with live vegetation, litter, and soil organic matter. The carbon absorbed by photosynthesis is partitioned into leaves, stems, and both fine and coarse roots. Stems and coarse roots also include both live and dead wood components that account for differences in respiration and the carbon:nitrogen ratio. The coupled nitrogen cycle in CHANGE allows consideration of nitrogen limitation on plant productivity, which therefore makes it possible to change the SOC decomposition rate that in turn affects productivity through nitrogen availability. The decomposition rates of SOC are controlled by soil temperature and moisture. These suppressions to the decomposition rate are also dependent on the root distribution.

2.2 Water tracer model

For simulation of water tracers, CHANGE employs an upstream isotopic scheme (Aleinov and Schmidt, 2006), additionally incorporating three water components (i.e., P_r, P_s, and P_i) as tracers. The scheme uses the water fluxes calculated by the LSM, and the advection of the tracers is performed as a sequence of two sweeps (i.e., up and down, indicating the direction of water flow). This allows simplification of the model calculation. As the water flux is directed downward, the tracers move to downstream cells with the water and mix immediately with tracers already in the cell. The tracer amount in that cell is then updated. The tracer amount in a cell is changed

only when water is added, and the same amount of tracer is retained until water is removed.

In the water cycle, precipitation and dew add water and tracer to the terrestrial system. The canopy layer primarily stores part of the precipitation, while evaporation and drip fall deplete the intercepted water. The latter in turn provides additional water and tracer to the snow or soil surface in the same way as throughfall. Water entering the soil layers sweeps down or up in the direction of water flow. The sweep-down-induced changes in tracer ($C_{i,t}$, kg m $^{-2}$) and water ($W_{i,t}$, m) at current time step (t) are computed as follows:

$$C_{i,t} = C_{i,t-1} - c_{i-1}F_{wi}\Delta t, \quad (1)$$

$$W_{i,t} = W_{i,t-1} - F_{wi}\Delta t, \quad (2)$$

where c_{i-1} (kg m^{-3}) is the concentration of tracer in the upper layer (i−1), F_{wi} is the water flux (m s^{-1}) from the upper layer, and Δt is the time step (s). Soil water content within the i-th soil layer is based on a finite difference approximation of the Richards equation. The moisture content (θ_i) of each layer is updated as:

$$\frac{d\theta_i}{dt} = F_{w,i-1} - F_{w,i} - ET_i, \quad (3)$$

where $F_{w,i-1}$ and $F_{w,i}$ are the diffusive water flux from the layer above and to the layer below, respectively, and ET_i is the ET extracted from the layer by plant roots and soil evaporation. The vertical water flux (F_w) in the soil layers is computed according to Darcy's law:

$$F_w = K_w \frac{\partial}{\partial z}(h + z), \quad (4)$$

where K_w is the hydraulic conductivity, z is a vertical coordinate, and h is the matric potential. The model performs a sweep down for i from 2 to n. In contrast, the sweep up starts from $i = n - 1$ and ends with $i = 1$:

$$C_{i-1,t} = C_{i-1,t-1} + c_i F_{wi} \Delta t, \quad (5)$$

$$W_{i-1,t} = W_{i-1,t-1} + F_{wi} \Delta t, \quad (6)$$

$$c_i = C_i / W_i. \quad (7)$$

After completion of both sweeps, the water associated with ET and runoff is removed from the soil layers and the amount of tracer is updated accordingly. The tracer concentration (C_{ei}) for evaporation from the canopy, snow, and soil surface is expressed as follows:

$$C_{ei,t} = C_{ei,t-1} + c_i \alpha F_{wi} \Delta t, \quad (8)$$

where F_{wi} represents the evaporative flux and α is the kinetic fractionation coefficient that is the function of wind speed (Merlivat and Jouzel, 1979). Moreover, α is alternated by an equilibrium fractionation coefficient (Majoube, 1971) because dew condenses on the surfaces of the canopy, snow, and soil. Additionally, Eq. (8) is equally used to calculate the changes of tracer concentration in E_t and runoff. The extraction of the tracers by plant roots in each soil layer is dependent on the LSM-estimated transpiration amount and the root fraction.

The CHANGE model uses a passive characteristic for the stable water isotopes, that is, there is no fractionation at any phase change in the soil or during transpiration and runoff. However, we assumed that evaporation of water from the wet canopy, snow, and soil surface fractionates the isotopes by the kinetic coefficient in Eq. (8), consequently enriching the isotope rates of the remaining water, whereas evaporative

fractionation was excluded from other water tracers by setting $\alpha = 1$. This assumption makes it possible to examine the differences in isotopic ratios in soil moisture, runoff, canopy water, and precipitation.

CHANGE calculates the water budget of individual elements (i.e., canopy, snow, and soil) in the LSM, where the water flux between elements is always directed downward. The tracer model that adopts the flow physics is applied separately to the elements. The update of the tracers starts from the canopy and then proceeds in sequence to the snow and the soil, depending on the water fluxes. In the model calculation, P_G is separated into P_r and P_s tracer members that provide the tracer inputs to the elements of the LSM. The tracers move with the water flux and mix completely with the previously stored tracers in individual elements. In the canopy or snow layer, the integrated amount of P_r and P_s is balanced by the stored water amount. In permafrost soil, P_i is added to the tracer member. Water in the permafrost soil experiences the phase change of seasonal freezing and thawing. Thus, P_i occurs during progression of the ALT (i.e., thawing). However, the occurrence of P_i in each soil layer is constrained to happen only once during the calculation period. When the ALT exceeds the maximum ALT identified during the calculation period, including the spin-up run, the ice-melted water at the soil layer is defined as P_i. Once P_i occurs, there is no additional P_i production from the soil layer. Therefore, P_i production is an inherent event in each soil layer. Although P_r and P_s experience seasonal freezing and thawing, the phase changes never affect the change of P_i.

2.3 Description of study site and observations

253 The observation site, which is underlain with continuous permafrost, is located
254 on the left bank of the middle reaches of the Lena River in eastern Siberia,
255 approximately 20 km north of Yakutsk. The site, which is called “Spasskaya Pad,” is
256 part of an experimental forest of the Institute for Biological Problems of Cryolithozone,
257 Siberian Branch of the Russian Academy of Sciences (SB-RAS). Climatologically
258 (1998–2010), the annual mean air temperature is −10.4°C and the annual mean P_G is
259 259 mm (Ohta et al., 2014). The dominant tree species of the overstory is 160-year-old
260 larch (*Larix cajanderi*) with mean tree height of 18 m, stand density of 840 trees ha^{-1},
261 and a leaf area index of 2.0. The forest floor is fully covered by dense cowberry
262 (*Vaccinium vitis-idaea*). The soil at the experimental site is classified as sandy loam. A
263 meteorological observation tower (height: 32 m) was installed at the site, where various
264 meteorological variables were measured at multiple heights. Two eddy-covariance
265 systems were installed at the top of the tower and at the height of 2 m above the forest
266 floor to monitor sensible and latent heat and CO_2 fluxes. Soil moisture and temperature
267 were measured at multiple depths (0–1.2 m) in the soil column. Full descriptions of the
268 site and observations were given by Kotani et al. (2019).

269 Cores of near-surface frozen and unfrozen soil down to 2.4-m depth were
270 sampled at three locations within a larch forest patch in Spasskaya Pad at the end of
271 March 2010. A powered auger (Tanaka TIA-350S) with a 2.5-inch-diameter core
272 sampler was used for the sampling. Sampled cores were truncated to remove
273 contamination, cut into vertical lengths (3–13 cm), and maintained in a frozen state in
274 vacuum-sealed plastic bags until required for laboratory analyses. The isotopic
275 compositions of water (hydrogen and oxygen) were analyzed using the $CO_2/H_2/H_2O$
276 equilibration method using a Delta V isotope ratio mass spectrometer (Thermo Fisher

277 Scientific, USA, manufactured in Germany) attached to a Gas Bench (Thermo Fisher
278 Scientific, USA) at Hokkaido University, Japan (Ueta et al., 2013). These data were
279 expressed as δ^2H or $\delta^{18}O$ values, defined as δ_{Sample} (‰) = ($R_{Sample}/R_{VSMOW} - 1$) × 1000,
280 where R is the isotope ratio of water ($^2H/^1H$ or $^{18}O/^{16}O$), and subscripts "Sample" and
281 "VSMOW" refer to the samples and standard (i.e., Vienna Standard Mean Ocean
282 Water), respectively. The analytical errors for the entire procedure were within 2‰ and
283 0.2‰ for δ^2H and $\delta^{18}O$, respectively. The analyzed isotope ratios of all samples within
284 each 30-cm depth were integrally averaged for comparison with the simulated values.
285
286 2.4 Model application
287 To create the daily model forcing data for the period 1980–2016, observations
288 at the study site were combined with ERA-Interim reanalysis data from the European
289 Centre for Medium-Range Weather Forecasts. These data include the bias-corrected
290 monthly Climate Research Unit temperature dataset and the Global Precipitation
291 Climatology Project precipitation dataset, which were used as the baseline to construct
292 the meteorological forcing data for running the model. Miyazaki et al. (2015) describe
293 the generation of the forcing data in detail.
294 CHANGE needs isotopic forcing data of P_G and atmospheric water vapor.
295 However, continuous, long-term observational records of such isotope data are lacking.
296 There is currently no alternative to a numerical model for preparing the isotopic forcing
297 data for running the model. The Scripps Isotopes-incorporated Global Spectral Model
298 (IsoGSM) has been used to produce a long-term global dataset of stable water isotopes
299 (Yoshimura et al., 2008). Thus, the results from the grid nearest to the experimental site
300 were selected and used as forcing data for CHANGE. However, the daily P_G events

between our forcing data and IsoGSM were found inconsistent, which would have likely resulted in uncertainties regarding the model simulation. Therefore, weighted monthly averages of the IsoGSM-simulated isotopic values of P_G and specific humidity were calculated, and the averaged values were applied homogeneously to the daily P_G and specific humidity. The monthly averaged isotopic values of the IsoGSM-simulated P_G were compared with records of observations taken at Yakutsk station over a 5-year period (1996–2000), archived as part of the Global Network of Isotopes in Precipitation by the International Atomic Energy Agency. The comparison revealed general overestimation by the IsoGSM for the two isotopic components (Fig. 1), which would likely cause uncertainty in the simulated isotopic processes. Therefore, the IsoGSM-simulated isotopic values used for the CHANGE simulations were adjusted to the observations using a scaling coefficient of 1.3.

A static land cover type of boreal deciduous needleleaf forest was defined for the simulation, while the vegetation phenology was prognostic based on estimated carbon and nitrogen fluxes. Measured fractions of sand, silt, and clay were set initially to those of the vertical soil texture profile, and the SOC profile was simulated at each time step. On the basis of these soil properties, the model estimated the thermal and hydraulic properties of the soil. Through the spin-up run, the model determined a dynamic equilibrium of total ecosystem carbon and nitrogen contents with the prescribed climate, repeating for 1200 years using the detrended forcing data of the initial 20 years and a CO_2 concentration of 350 ppm. After completing the spin-up, the atmospheric CO_2 concentration in the simulations was set to vary over time based on global observational records. The minimum oxygen (−25‰) and hydrogen (−190‰) isotopic values obtained from the analyzed soil cores were set as the initial isotope

values of all the soil layers. The stable water isotopes of the soil layers were updated through mixing with the P_G inputs and evaporation fractionation during the spin-up period. Ultimately, the influence of the initialization on the simulated results was minor, at least in the active layers.

Plant roots extract soil moisture, resulting in a vertically heterogeneous water profile. The root profile readily affects soil moisture as well as tracer amounts. To explore how different root profiles might affect E_t and the tracers, three numerical experiments were designed. In the control simulation (S_{CN}), the cumulative root distribution was given by $(1 - \beta^z)$, where z is the soil layer thickness and β is a vegetation-dependent coefficient (Jackson et al., 1996), which is assumed time invariant. As β does not change with vegetation age and/or root biomass, the rooting depth remains constant irrespective of plant size. The second simulation (S_{MT}) used the root algorithm adopted from Williams et al. (2001). In this algorithm, plant root distribution is determined by three factors: the time-variant total fine root biomass, maximum root biomass per unit volume that is assumed to occur at the soil surface, and depth of rooting. The root biomass per unit volume decays exponentially in terms of root length with depth. The third simulation (S_{AB}) was based on the model of Arora and Boer (2003), which proposed a methodology for parameterizing root distribution as a function of root biomass. The S_{AB} model is intended to overcome some of the limitations in the prescription of a static root distribution profile in dynamic vegetation models. In the representation, root distribution and rooting depth both evolve and increase as the root biomass increases, as would be expected intuitively. The soil column (70.4 m) in CHANGE is discretized into 31 layers. The soil surface (e.g., ~0.37 m) over which the soil water gradient is generally strong forms six soil layers based on

an exponential equation (Oleson et al., 2010), and then the soil layers have a 0.2-m node depth to 3.2 m. The deepest remnant layers in turn form thicker node depths based on the exponential equation.

3. Results

3.1 Model performance

The CHANGE-simulated results for energy, water, and carbon fluxes, *ET*, and soil moisture and temperature profiles, which have previously been validated against observational records, showed statistically satisfactory performance for seasonal and interannual variability in different climatic zones, including the Spasskaya Pad study site (Park et al., 2011, 2018). Here, the validation of model performance using observations was confined to the simulated isotopic results because the isotope process was newly coupled to the model. The model-simulated soil-isotope profiles were averaged for March 2010 when the soil cores were sampled. The monthly averaged simulations were compared with the median values of the analyzed soil cores (Fig. 2). The three simulations that have vertically different root distributions (Fig. 2c) show similar profiles from the surface to the depth of 2.4 m (Fig. 2a, b). The comparison indicates that the simulated isotope ratios (i.e., $\delta^{18}O$ and $\delta^{2}H$) distribute within or close to the interquartile range (IQR) of the observations from the surface to 1.2 m (Fig. 2a, b), where the observed and simulated isotope ratios are depleted with depth. However, at depths of 1.2–1.8 m, where soil moisture is generally saturated owing to permafrost table blocking of water infiltration, the model simulated enriched isotopes in comparison with the observations of depletion with depth. CHANGE tends to estimate

372 higher hydraulic conductivity and porosity owing to the SOC and vertically consistent
373 soil texture composition. The higher hydraulic conductivity likely enhances the mixing
374 of summer P_G-originated heavy isotopes in the ALT.

375 A previous study provided oxygen isotopic ratios of soil water in three soil
376 layers and of sap water in plants sampled during the growing season during 1998–2000
377 at the same study site (Sugimoto et al., 2003). We used the analyzed isotope ratios of
378 two soil layers (0–0.3 and 0.3–0.6 m) and sap water for further validation of the
379 simulations. The modeled isotope ratios were averaged for 10 days prior to the
380 observation date. Although comparison of the surface soil water (Fig. 2d) shows
381 agreement between the simulations and observations, larger deviations are specifically
382 identified at the three simulated events (e.g., August and September 1999 and May
383 2000). The deviations are partially attributable to the influence of biased monthly
384 precipitation isotopic forcing; for example, the model was forced by precipitation of
385 −19.9‰ in August 1999, which was lighter than observed, that is, −15.7 ‰ (Sugimoto
386 et al., 2003). The P_G isotopic ratios for the CHANGE simulations were corrected for
387 bias using the observed values; however, some deviations remained. The deviations in
388 the surface soil layer that had the largest fraction of roots (Fig. 2c) were consequently
389 associated with errors (−2.2‰, root mean square error) in transpiration (Fig. 2f).

390

391 3.2 Impacts of separated source waters on evapotranspiration

392 The simulated daily vertical soil moisture and separated source waters were
393 averaged for the entire study period, and the averaged seasonal variability is presented
394 in Fig. 3. In spring, the frozen soil thaws and saturates the soil surface (Fig. 3a) with the

395 inflowed P_s (Fig. 3b). The derived P_s, which is mainly stored in the surface soil layers,
396 that is, to approximately 10-cm depth during April–June (Fig. 3b), is also pushed down
397 by incoming summer P_r during the same period and contributes to the higher level of
398 soil moisture at the depth of 0.8 m or deeper (Fig. 3a). The P_r from the previous autumn
399 that exists in the upper layers is displaced by the incoming P_s and flows downward,
400 partially infiltrating to depths of 2.0 m (Fig. 3c). The surface soil moisture is sourced
401 primarily from summer P_r of the current year, whereas the deeper soil contains waters
402 of varying ages. In autumn, the fraction of P_r in the surface soil moisture increases
403 owing to low evaporation and transpiration, and this higher level of soil moisture is
404 maintained until the following spring. Overall, P_i is primarily distributed at the depth of
405 1.7–2.1 m (Fig. 3d), reflecting the signal of the ALT progression during the simulation
406 period.

407 Snow meltwater is distributed mainly from the surface to 10-cm depth during
408 spring, accounting for 40% or more of the gross soil moisture, whereas the fraction in
409 deeper layers is considerably lower. Overall, the main source of soil moisture within the
410 ALT is P_r, which accounts for 80% or more over the entire period, except in the surface
411 layers in spring. The maximal fraction of 95% occurs in the surface layers owing to
412 autumnal rainfall. Overall, P_i at depths of 1.7–2.1 m accounts for approximately 10% of
413 the soil moisture.

414 The averaged seasonal variations of *ET* and the subcomponents with the
415 contribution amounts of the separated source waters are displayed in Fig. 4. It can be
416 seen that *ET* shows typical seasonality with a summer peak, consistent with E_t that
417 accounts for 63.3% of *ET* (Table 1). Temporally, E_t increases rapidly with leaf opening
418 and the increase of T_a, reaching the maximum value in July, which is different to the

419 gradual increase of E_i. Approximately 60% of E_i is apportioned by rainfall (Table 1).
420 Meanwhile, E_s increases from early spring (when the frozen soil begins to thaw),
421 reaches the maximum value in May, and thereafter decreases markedly owing to the
422 reduction in solar radiation induced by the increasing leaf amount. The maximal value
423 of E_s in spring is a general phenomenon in cold regions (Park et al., 2008).

424 The source waters that contribute to E_s show interesting seasonal variations. In
425 spring, E_s simultaneously evaporates P_r and P_s from the soil surface (Fig. 4c). When P_s
426 covers the soil surface, evaporation of P_r is temporally restrained. During April–May,
427 P_s accounts for 47% of E_s. Once the P_s in the soil surface is largely evaporated,
428 evaporation of P_r restarts and accounts for most of E_s during summer. In summer, the P_s
429 that enters the surface soil layers (Fig. 3b) is transpired by plants; however, the
430 contribution of P_s to E_t is not larger than that of P_r, which accounts for 85.7% of E_t
431 (Table 1). The largest uptake of P_r by plants occurs in the soil layers in which the roots
432 are fractionally maximal (Fig. 5). The three experiments show evident differences in the
433 vertical distribution of E_t. The maximal E_t values in individual experiments are present
434 at the same soil layers that the root fraction is maximal (Fig. 2c). For example, S_{CN}
435 presents the maximal value of E_t at 10-cm depth, whereas it is at 40-cm depth in S_{MT}.
436 Uptake of water by plant roots is strongest in June and July (Fig. 5) when plant
437 productivity is most vigorous (Park et al., 2011). However, the difference in the annual
438 E_t between the three experiments that show vertically different root profiles is not large
439 (Table 1). Overall, P_r accounts for 80.1% of ET (Table 1). The contribution of P_i to ET
440 is negligible because P_i is stored mainly in the deepest soil layers (Fig. 3d) where roots
441 are nonexistent (Fig. 2c).

442

3.3 Isotope variability

The simulated isotopes in the soil column were averaged over the study period, and their seasonal and vertical variations are displayed in Fig. 6. Both $\delta^{18}O$ and $\delta^{2}H$ show similar seasonal variation in their vertical profiles and evident delineation of the signal of the translatory flow of water movement; in other words, P_G-originated water entering the soil displaces the water that is already present, pushing it deeper into the soil (Hewlett and Hibbert, 1967; Horton and Hawkins, 1965). In spring, the inflowing P_s displaces the water resident in the surface layers and depletes the isotope ratios. Then, the downward movement of the surface water enriches the isotopes of the soil below. Meanwhile, the P_r-induced translatory flow in summer isotopically depletes the deeper soil via the inflow of P_s from the surface layers. In turn, the autumn P_r depletes the isotopes of the surface soil, and the resultant isotope ratios in autumn remain until the following spring. The d-excess also displays similar seasonal variability to that identified in relation to $\delta^{18}O$ and $\delta^{2}H$. Isotopically enriched summer P_G results in the lowest d-excess in the upper soil layers, and the kinetic fractionation with evaporation also contributes to the lowest d-excess in the surface layer (Fig. 6c).

Winter P_G results in the lowest value of $\delta^{18}O$ for the snowpack (min.: −33‰) (Fig. 7a). The surface soil water is displaced by the melted P_s, resulting in a depleted $\delta^{18}O$ value in late April (Fig. 7a), which is eventually linked to the depleted E_s $\delta^{18}O$ (Fig. 7b) owing to the largest loss of P_s by E_s (Fig. 4c). Then, E_s $\delta^{18}O$ is enriched during summer under the influence of heavy P_r $\delta^{18}O$ before returning to a more depleted level in autumn (Fig. 7a). Meanwhile, E_t $\delta^{18}O$ generally evolves toward summer (Fig. 7b) because E_t preferentially uses the isotopically light and stable moisture of deeper soil layers (Fig. 5) owing to the relatively large fraction of roots (Fig. 2c). The influence of

467 P_s on the isotopes of E_t is not large, causing instead slightly depleted $\delta^{18}O$ in May (Fig.
468 7b). The median of the monthly averaged E_t $\delta^{18}O$ (−19.5‰) is similar to that of soil
469 water in the surface layers (−19.3‰), with similar variability expressed by an IQR of
470 1.1% and 1.9%, respectively (Fig. 8), indicating stronger hydrological connectivity
471 between them. Meanwhile, the simulated homogeneous isotope ratios in soil water at
472 depths of 0.3–1.4 m (Figs. 2 and 6) likely result in a relatively small IQR for E_t $\delta^{18}O$.
473 The distributions of E_t $\delta^{18}O$ in the boxplots (Fig. 8) indicate a range of −21.1‰
474 (minimum) to −17.2‰ (maximum), which is generally consistent with the range
475 −22.5‰ to −16.0‰ observed in sap water during 1998–2000 at the same site (Sugimoto
476 et al., 2003).

477 Canopy-intercepted water shows the largest IQR (i.e., 13.4%) for $\delta^{18}O$ (Fig. 8),
478 representing the variability caused by both the isotopic depletion by condensation in the
479 cold season and the enrichment of heavy isotopes by evaporation fractionation in
480 summer. Snowpack shows more depleted isotopes and thus a lower median value
481 (−31.1‰ for $\delta^{18}O$) than P_G (−28.7‰), and it plots outside the median values of other
482 processes (i.e., E_s, E_t, and soil water). However, the minimum value of snowpack in the
483 boxplot is larger than that of P_G and canopy water (Fig. 8), indicating isotope
484 enrichment by sublimation fractionation from the snow surface and the addition of
485 isotopically enriched snow falling from the canopy. The signal of evident enrichment of
486 the median $\delta^{18}O$ from P_G to soil water confirms the effects of evaporation and water
487 mixing in the hydrological processes on the isotope changes (Ala-aho et al., 2018).

488 Signals of evaporation in hydrological processes can be explored using d-
489 excess values. The d-excess median for water storages (i.e., canopy, snow, and soil)
490 tends sequentially to reduce along the water flow from P_G to the soil system, plotting

491 below the median of P_G d-excess, and the d-excess values in ET (E_i, E_s, and E_t), closely
492 associated with summer P_G, are also lower (Fig. 8). Overall, E_s has the lowest d-excess
493 values (median: −1.5‰), indicating a strong evaporation signal. The snowpack d-
494 excess, averaged over the cold season from autumn to spring (8.7‰), is lower than the
495 median value of 11.8‰ observed in the coldest February/March in Siberian regions
496 (Kurita et al., 2005; Vasil'chuk et al., 2016; Ala-aho et al., 2018), despite the lower
497 isotopic ratios (i.e., −31.1‰ for $\delta^{18}O$) than observed (i.e., −28.8‰ for $\delta^{18}O$) (Vasil'chuk
498 et al., 2016). The volume-weighted average of P_G d-excess is 12.4‰ (Fig. 8), which is
499 higher than the value (2.9‰) of the Global Network of Isotopes in Precipitation samples
500 from Yakutsk. The local meteoric water line—the regression line of all processes in
501 Fig. 8—has slope of 7.90, similar to that (7.81) of precipitation samples from Yakutsk
502 obtained from the Global Network of Isotopes in Precipitation.
503
504 3.4 Interannual variability of evapotranspiration
505 In cold regions, T_a is a major driving factor for ET. The simulated ET shows an
506 increasing trend (0.18 mm yr^{-1}, $p < 0.10$) during 1980–2016 (Fig. 9), which is a
507 response to the increasing T_a (Fedorov et al., 2014). Overall, ET averaged for the three
508 experiments during the study period was 187 mm yr^{-1} (Table 1), which explained 95%
509 of the observed annual mean ET (196 mm) for 1998–2006 (Park et al., 2011). The
510 subcomponents of ET increase consistently, although they are statistically insignificant.
511 The increase of T_a causes greater plant productivity and a larger leaf area index (Park et
512 al., 2011) associated with the higher E_t and water storage on leaf surfaces, leading to
513 higher E_i. Meanwhile, the larger leaf area decreases solar radiation at the forest floor,

514 consequently reducing E_s with an insignificantly negative trend of −0.005 mm yr^{-1}.
515 Observations have identified earlier thawing of frozen soil (Kim et al., 2015; Fedorov et
516 al., 2014) correlating to larger E_s. Therefore, the climate-warming-induced decrease of
517 solar radiation and earlier onset of soil thawing have a competitive relationship
518 regarding E_s. The contribution of P_r to ET increased significantly during the study
519 period (0.23 mm yr^{-1}, $p < 0.01$), whereas that of P_s decreased slightly (−0.005 mm yr^{-1},
520 statistically insignificant).

521

522 3.5 Sensitivity analysis

523 The three experiments characterized by vertically different root profiles
524 resulted in small difference in the annual E_t; S_{MT} with the deepest root depth (Fig. 2c)
525 transpired 3 mm more soil water than either S_{CN} or S_{AB} (Table 1). To investigate the
526 influence of root depth on E_t, two sensitivity experiments with root depth extending to
527 1.56 m were conducted based on the parameters and conditions of S_{CN}. Specifically, the
528 first experiment excluded the soil freezing stress by permafrost for plant roots
529 connected to photosynthesis and stomatal conductance (S_{TE}), whereas the second
530 experiment did consider the stress (S_{TI}). The sensitivity experiments produced E_t values
531 of 117.5 mm for S_{TE} and 117.2 mm for S_{TI}, showing similar values to S_{CN} (Table 1)
532 despite the large differences in root depth. The CHANGE-simulated ALT was in the
533 range of 1.5–1.8 m in all experiments, in which the soil moisture within the ALT was
534 generally high (Fig. 3a). These conditions make plant roots free from the stresses of
535 both permafrost-related freezing and low soil moisture. Although the root length was
536 extended, the root fraction in the deepest soil layers was very low. Therefore, the impact

of extended roots on E_t was not large. In temperate or tropical regions where soil drought is frequent, root extension to deeper soil depths is efficient for E_t absorbing water from the deepest soil layers (Yang et al., 2016).

CHANGE also simulated isotope profiles in the three experiments that were similar to the observations in March 2010 (Fig. 2a, b). However, a difference between the simulations was found in the surface soil layers of 0–30 cm, in which S_{CN} with the largest root fraction produced slightly enriched isotopic values relative to S_{MT} and S_{AB}, suggesting possible impact of the root structure on isotope variability. Thus, the isotopic value of S_{CN} was in turn compared with that of S_{TE} and S_{TI}. In comparison with S_{CN}, the anomalous $\delta^{18}O$ profiles in S_{TE} and S_{TI} show enriched isotopic values in all soil layers except the surface layer (Fig. 10). The deepened roots of S_{TE} and S_{TI} absorbed further water despite having a lower root fraction in the deeper layers, driving more downward mobility of isotopically heavy water from the upper soil layers. The resultant inflow of summer precipitation-originated warm water to the lower soil layers increased the ALT; consequently, the ALT of S_{TE} and S_{TI} was 10 cm deeper than that of S_{CN}. The water movement during ALT development caused an increase in heavy isotope ratios in the deepest soil layers (Fig. 10). These results indicate a hydrological function of the root structure associated with the fluxes of soil water.

4. Discussion

Previous large-scale hydrological work focused on high-latitude landscapes has successfully isolated the volumetric contributions of snowmelt, groundwater, and summer rainfall to streamflow, and established relationships between seasonal water

560 balance components and climatic variables (Serreze et al., 2002; Ye et al., 2004; Yang
561 et al., 2004; Tan et al., 2011). The results revealed representatively that P_s is the
562 dominant runoff generation process, accounting for approximately 60% in the Kolyma
563 watershed of northeastern Siberia that is underlain by continuous permafrost (Welp et
564 al., 2005) and in the Yukon (Canada) and Alaska (USA) (Lachniet et al., 2016). Unlike
565 its identified impact on runoff, the influence of P_s on *ET* has yet to be fully assessed.
566 Here, we provide quantitative evidence that P_s accounts for 14%–40% of *ET* and the
567 subcomponents (Table 1) in eastern Siberia, that is, considerably lower in comparison
568 with runoff. When snow melts, the underlying soil remains frozen and the ALT is low.
569 While frozen soil promotes rapid routing of P_s in a landscape generating infiltration-
570 excess surface runoff (Woo et al., 2008), part of P_s wets the surface soil (Fig. 3) and
571 thus contributes to *ET*. The distribution of $\delta^{18}O$ presents lower probability for utilization
572 of a snow-derived isotopically lighter water by E_s and E_t than reliance on heavier water
573 derived from summer rainfall (Fig. 11).

574 As *ET* occurs primarily during the warming season, the influence of summer
575 rainfall on *ET* is intuitively large. At the study site, rainfall that accounted for 65% of
576 annual P_G showed a trend of increase (0.61 mm yr^{-1}, $p < 0.1$) during the study period.
577 Increased rainfall primarily reduces the limitations of moisture availability for *ET*. In
578 addition, a warming climate induces a longer growing season (Kim et al., 2015; Park et
579 al., 2016) that is beneficial for enhanced *ET*. Summer rainfall tends to be stored in
580 surface soil layers (Fig. 3) with high porosity owing to the effects of SOC, and the water
581 is extracted immediately by the higher fraction of roots (Fig. 2c). In turn, rainfall events
582 supply water to the dried surface layers, and this water is generally of relatively young
583 age with isotope ratios similar to those of P_G (Fig. 6), identified by the higher use of an

584 isotopically heavier source water by E_s in the summer (Fig. 11) and thus lower d-excess
585 (Fig. 8). Owing to the larger water consumption in the surface soil layers, summer
586 rainfall has comparatively low opportunity to exchange with water of the deeper soil.
587 Thus, we did not find signals of significant isotopic enrichment as evidence of the
588 largest movement of summer rainfall into the deeper soil in the control simulation (Fig.
589 6). The smaller isotope changes of soil moisture resulted in a tight distribution of E_t
590 $\delta^{18}O$ of between −22‰ and −16‰ (Fig. 11) with the steady state flux during the
591 growing season (Fig. 7b). However, the extension of root depth caused isotopic
592 enrichment at the deeper soil layers because root water uptake induces water inflow
593 from the upper layers (Fig. 10). This is likely amplified by larger root biomass and ALT
594 under a warming climate, including further implication of P_i to soil water flux and E_t.

595 Previous studies have examined the impact of autumn P_G on permafrost
596 warming via snow insulation (Park et al., 2015), as well as its connectivity to spring
597 streamflow via lake and wetland water storage (Hayashi et al., 2004). However,
598 understanding the physics of how autumn rainfall that is generally stored in the surface
599 layers as frozen water (Fig. 3c) is related to *ET* in the following summer and its
600 quantitative assessment is lacking. Here, our tracer model illustrated a physical
601 mechanism via which autumn rainfall is connected to the ecohydrological processes of
602 the following summer. In autumn, the soil generally becomes frozen before the
603 autumnal rainfall infiltrates into the deeper soil. Therefore, autumn rainfall spends the
604 winter as ice in the upper soil layers. Part of the autumn rainfall is used directly by E_s
605 during snow melting (Fig. 4). The entering P_s pushes the autumn rainfall in the surface
606 soil layers downward (Fig. 6). The downward movement of autumn rainfall contributes
607 to spring soil wetness (Fig. 3a) and then to higher summer *ET*. Strictly, the flux of

608 spring P_s enhances the mixing of autumn rainfall with the existent soil water in the
609 deeper layers and then connects to the summer *ET*. Unfortunately, the tracer model
610 remains deficient in illustrating the entire pathway via which water of each P_G event
611 leaves the surface–subsurface system as streamflow or *ET*. Therefore, the tracer model
612 cannot provide information on the quantitative contribution of seasonal P_G to *ET*, which
613 will be addressed in future research.

614 The progress of the ALT reflects the melting of ground ice in the permafrost
615 table. In this study, P_i comprised approximately 10% of the soil moisture in the lower
616 ALT boundary layer (Fig. 3). As P_i is located below the root depth, access to P_i by
617 plants is considerably restricted. Consequently, we found nearly no contribution to E_t by
618 P_i. Under dry conditions, plants extract water from deeper soil layers to reduce moisture
619 stress (Nepstad et al., 1994; Yang et al., 2016). The study site has a dry climate owing
620 to the reasonably low P_G. However, soil moisture within the ALT generally maintains
621 wet conditions beyond the wilting point (Fig. 3a). Thus, this soil moisture likely reduces
622 the dependence of *ET* upon the P_i of the deeper soil. The deeper soil layers in which P_i
623 is stored usually record soil temperatures close to 0°C. The cold temperature likely
624 limits the activity of water extraction by roots. Indeed, the S_{MT} experiment with the
625 deepest root depth of 1.0 m resulted in annual E_t that was 3 mm greater than in S_{AB} with
626 the shallowest root depth (Table 1), suggesting relatively low impact of the different
627 root profiles on annual E_t between the wet and cold permafrost regions. However,
628 LSMs have projected dry soil moisture in the Arctic regions under the conditions of
629 future climate change (Andresen et al., 2020); therefore, we expect that the contribution
630 of P_i to E_t will probably increase further.

631 The tracer model is a powerful tool with which to represent more
632 comprehensively the physical dynamics of P_G-originated waters and the isotopes in the
633 surface–subsurface system. The simulated isotope variations present a seasonal shift in
634 the reliance of *ET* on an isotopically lighter water supply in spring, followed by a
635 transition toward the use of an isotopically heavier source water in summer (Fig. 7). In
636 particular, the soil surface layers in early spring have experienced strong mixing of P_s
637 and P_r, showing their competitive contributions to E_s during the shortest period (Fig.
638 4c). CHANGE simulated the deficient isotope values in the phase of P_s priority for E_s
639 and soil water and then their enrichment governed by P_r (Fig. 7). This simulation
640 alternatively supports a reasonable estimation of the partition of P_G-originated *ET*
641 source waters (Fig. 4), seldom validated by observational data. For the model
642 calculation, isotopic forcing data are required to drive the tracer module. However, few
643 in situ long-term observational data are currently available. Alternatively, we used
644 monthly isotopic ratios produced by an isotope climate model as the forcing. The use of
645 monthly isotopic data was probably inappropriate for realistic representation of the
646 concentration changes of the isotope compositions in each P_G event. Nevertheless, as
647 the main work of this study does not complete the transpiration–evaporation
648 partitioning based on the simulated isotope ratios, uncertainties related to the monthly
649 forcing data might not preclude meaningful analysis on the separation of the source
650 waters used for *ET*. Furthermore, the model did appropriately simulate the isotopic
651 composition changes through mixing, advection, diffusion, and related fractionation in
652 water transport in the surface–subsurface continuum.

653 Previous studies have identified dual water flows in the soil system, that is,
654 water moves slowly through soil micropores and rapidly through preferential pathways

655 that bypass the soil matrix (McDonnel, 1990; Buttle and McDonald, 2002; Hrachowitz
656 et al., 2013, 2016). Unlike previous findings, our tracer model assumed that tracer
657 transport was proportional to the water flux and that complete mixing occurred in each
658 soil layer. Homogeneous mixing likely results in earlier arrival of tracers to a certain
659 depth with a more dispersed transit time distribution than observed (Hu et al., 2018).
660 Consequently, the model assumptions could increase the influence of incoming tracer
661 flux on changes in tracer concentrations. For example, the simulated isotope ratios
662 showed large deviations against observations at 1.2–1.8-m depth (Fig. 2a, b). The
663 deviation is probably an example associated with the model assumptions, combined
664 with the influence of the monthly isotopic forcing data. To represent physically the
665 heterogeneous water flow, Hu et al. (2018) introduced a parameterization of a
666 dynamical partial mixing by separating the total storage in each soil layer into
667 active/mobile and passive/immobile compartments, and the model appropriately
668 implemented the ecohydrological separation of soil water found by isotopic studies
669 (Brooks et al., 2010; Evaristo et al., 2015). The parameterization suggested by Hu et al.
670 (2018) represents a reasonable benchmark with which to assess improvement of the
671 deficiency of our tracer model.

672

673 **5. Conclusions**

674 We developed a water tracer model specifically designed to estimate the
675 storage and fluxes of P_G- and permafrost-originated waters of individual
676 hydrometeorological events based on changes in isotopic concentration via water
677 transport. In comparison with existing LSMs that incorporate isotopes, our tracer model

678 explicitly separates the contributions of the partitioned tracers to water balance
679 components. The model implementation considers that P_r is the major contributor to ET
680 in a deciduous needleleaf boreal forest, while the contribution of P_s is acknowledged as
681 restrictively significant to E_s and E_t in early summer because of the blocking effect of
682 permafrost on water infiltration. The simulated isotope ratios contribute to reduction of
683 uncertainties regarding the separate contributions of P_G-originated source water to ET,
684 which have yet to be validated with observed data. Future climate warming will induce
685 earlier and deeper soil thawing that will likely increase the quantity of P_s entering the
686 soil and hence result in a larger contribution to ET. By contrast, the warming climate
687 will increase the fraction of summer rainfall in P_G (Bintanja and Andry, 2017), which
688 will also contribute to larger ET. We therefore expect that P_r will remain the largest
689 influence on ET in the future. The future climate could potentially increase the roles of
690 permafrost-related water in ecohydrological processes, but our understanding of which
691 remains considerably lacking. The presented water tracer model is certainly a useful
692 tool with which to distinguish quantitatively the changes of the water dynamic physics
693 caused by climate change.

694

695 **Acknowledgments**

696 This study was partly supported by the Japan Society for the Promotion of Science
697 KAKENHI Grant Number 17H01870 and 19H05668. It was also supported by JST
698 Belmont Forum Grant Number JPMJBF2003, Japan. We thank James Buxton MSc
699 from Edanz Group (https://en-author-services.edanz.com/ac) for editing a draft of this
700 manuscript. Data analyzed in this study will be opened through the data archive system
701 of JAMSTEC.

702

703 **References**

Ala-aho, P., C. Soulsby, O. S. Pokrovsky, S. N. Kirpotin, J. Karlsson, S. Serikova, S. N. Vorobyev, R. M. Manasypov, S. Loiko, and D. Tetzlaff, 2018: Using stable isotopes to assess surface water source dynamics and hydrological connectivity in a high-latitude wetland and permafrost influenced landscape. *J. Hydrol.*, **556**, 279–293, https://doi.org/10.1016/j.jhydrol.2017.11.024.

Aleinov, I., and G. A. Schmidt, 2006: Water isotopes in the GISS ModelE land surface scheme. *Global Planet. Change*, **51**, 108–120.

Andresen, C. G., D. M. Lawrence, C. J. Wilson, A. D. McGuire, C. Koven, K. Schaefer, E. Jafarov, S. Peng, X. Chen, I. Gouttevin, E. Burke, S. Chadburn, D. Ji, G. Chen, D. Hayes, and W. Zhang, 2020: Soil moisture and hydrology projections of the permafrost region – a model intercomparison. *Cryosphere*, **14**, 445–459, https://doi.org/10.5194/tc-14-445-2020.

Aora, V. K., and G. J. Boer, 2003: A Representation of Variable Root Distribution in Dynamic Vegetation Models. *Earth Interact.*, 7, 1–19, https://doi.org/10.1175/1087-3562(2003)007<0001:AROVRD>2.0.CO;2.

Bekryaev, R. V., I. V. Polyakov, and V. A. Alexeev, 2010: Role of polar amplification in long-term surface air temperature variations and modern Arctic warming. *J. Clim.*, **23**, 3888–3906.

Bintanja, R., and O. Andry, 2017: Towards a rain-dominated Arctic. *Nature Clim. Change*, **7**, 263–267, https://doi.org/10.1038/nclimate3240.

Brooks, J. R., H. R. Barnard, R. Coulombe, and J. J. McDonnell, 2010: Ecohydrologic separation of water between trees and streams in a Mediterranean climate. *Nature Geosci.*, **3**, 100–104, https://doi.org/10.1038/ngeo722.

Buttle, J. M., and D. J. McDonald, 2002: Coupled vertical and lateral preferential flow on a forested slope. *Water Resour. Res*, **38**, 1060, https://doi.org/10.1029/2001WR000773.

Evaristo, J., S. Jasechko, and J. J. McDonnell, 2015: Global separation of plant transpiration from groundwater and streamflow. *Nature*, **525**, 91–94, https://doi.org/10.1038/nature14983.

Fedorov, A. N., R. N. Ivanova, H. Park, T. Hiyama, and Y. Iijima, 2014: Recent air temperature changes in the permafrost landscapes of northeastern Eurasia. *Polar Sci.*, **8**, 114–128, https://doi.org/10.1016/j.polar.2014.02.001.

Fischer, M. J., 2006: iCHASM, a flexible land-surface model that incorporates stable water isotopes. *Global Planet. Change*, **51**, 121–130.

738 Gibson, J. J., and T. W. D. Edwards, 2002: Regional water balance trends and
739 evaporation-transpiration partitioning from a stable isotope survey of lakes in northern
740 Canada. *Global Biochem. Cycles*, **16**, 1026, doi:10.1029/2001Gb001839.
741 Goldsmith, G. R., L. E. Munoz-Villers, F. Holwerda, J. J. McDonnell, H. Asbjornsen,
742 and T. E. Dawson, 2012: Stable isotopes reveal linkages among ecohydrological
743 processes in a seasonally dry tropical montane cloud forest. Ecohydrol., 5, 779–790,
744 https://doi.org/10.1002/eco.268.
745 Good, S. P., D. Noone, and G. Bowen, 2015: Hydrologic connectivity constrains
746 partitioning of global terrestrial water fluxes. *Science*, **349**, 175–177.
747 Hayashi, M., W. L. Quinton, A. Pietroniro, and J. J. Gibson, 2004: Hydrologic functions
748 of wetlands in a discontinuous permafrost basin indicated by isotopic and chemical
749 signatures. *J. Hydrol.*, **296**, 81–97.
750 Hewlett, J. D., and A. R. Hibbert, 1967: Forest Hydrology (eds. Sopper W E & Lull H
751 W) .Pergamon, 275–291.
752 Horton, J. H., and R. H. Hawkins, 1965: Flow path of rain from soil surface to water
753 table. *Soil Sci.*, **100**, 377–383.
754 Hrachowitz, M., H. Savenije, T. A. Bogaard, D. Tetzlaff, and C. Soulsby, 2013: What
755 can flux tracking teach us about water age distribution patterns and their temporal
756 dynamics?. *Hydrol. Earth Syst. Sci.*, **17**, 533–564, https://doi.org/10.5194/hess-17-533-
757 2013.
758 Hrachowitz, M., P. Benettin, B. M. van Breukelen, O. Fovet, N. J. K. Howden, L. Ruiz,
759 Y. van der Velde, and A. J. Wade, 2016: Transit times-the link between hydrology and
760 water quality at the catchment scale. *Wiley Interdiscip. Rev.: Water*, **3**, 629–657,
761 https://doi.org/10.1002/wat2.1155.
762 Hu, H., F. Dominguez, P. Kumar, J. McDonnell, and D. Gochis, 2018: A numerical
763 water tracer model for understanding event-scale hydrometeorological phenomena *J.*
764 *Hydrometeor.*, **19**, 947–967.
765 Iijima, Y., T. Nakamura, H. Park, Y. Tachibana, and A. N. Fedorov, 2016:
766 Enhancement of Arctic storm activity in relation to permafrost degradation in eastern
767 Siberia. *Int. J. Climatol.*, **36**, 4265–4275, https://doi.org/10.1002/joc.4629.
768 Jackson R. B., J. Canadell, J. R. Ehleringer, H. A. Mooney, O. E. Sala, and E. D.
769 Schulze, 1996: A global analysis of root distributions for terrestrial biomes. *Oecologia*,
770 **108**, 389–411.
771 Jasechko, S., Z. D. Sharp, J. J. Gibson, S. J. Birks, Y. Yi, and P. J. Fawcett, 2013:
772 Terrestrial water fluxes dominated by transpiration. *Nature*, **496**, 347–350.

773 Jasechko, S., J. W. Kirchner, J. M. Welker, and J. J. McDonnell, 2016: Substantial
774 proportion of global streamflow less than three months old. *Nat*. *Geosci*., **9**, 126–129,
775 https://doi.org/10.1038/ngeo2636.
776 Kim, Y., J. S. Kimball, D. A. Robinson, and C. Derksen, 2015: New satellite climate
777 data records indicate strong coupling between recent frozen season changes and snow
778 cover over high northern latitudes. *Environ*. *Res*. *Lett*., **10**, 084004, doi:10.1088/1748-
779 9326/10/8/084004.
780 Kotani, A., A. Saito, A. V. Kononov, R. E. Petrov, T. C. Maximov, Y. Iijima, and T.
781 Ohta, 2019: Impact of unusually wet permafrost soil on understory vegetation and CO_2
782 exchange in a larch forest in eastern Siberia. *Agric. For. Meteorol*., **265**, 295–309,
783 https://doi.org/10.1016/j.agrformet.2018.11.025.
784 Kurita, N., A. Sugimoto, Y. Fujii, T. Fukazawa, V. N. Makarov, O. Watanabe et al.,
785 2005: Isotopic composition and origin of snow over Siberia. *J. Geophys*. *Res*., **110**,
786 D13102, https://doi.org/10.1029/2004JD005053.
787 Lachniet, M. S., D. E. Lawson, H. Stephen, A. R. Sloat, and W. P. Patterson, 2016:
788 Isoscapes of δ18O and δ2H reveal climatic forcings on Alaska and Yukon precipitation.
789 Water Resour. Res., 52, 6575–6586, https://doi.org/10.1002/2016WR019436.
790 Majoube, M., 1971: Oxygen-18 and deuterium fractionation between water and steam
791 (in French). *J. Chim*. *Phys*. *Phys*-*Chim*. *Biol*., **68**, 1423–1436.
792 McGuire, K. J., J. J. McDonnel, M. Weiler, C.Kendall, B. L. McGlynn, J. M. Welker,
793 and J. Seibert, 2005: The role of topography on catchment-scale water residence time.
794 *Water Resour*. *Res*., **41**, https://doi.org/10.1029/2004WR003657.
795 McDonnel, J. J., 1990: A rationale for old water discharge through macropores in a
796 steep, humid catchment. *Water Resour*. *Res*., **26**, 2821–2832,
797 https://doi.org/10.1029/WR026i011p02821.
798 Merlivat, L., L. Jouzel, 1979: Global climatic interpretation of the deuterium oxygen 18
799 relationship for precipitation. *J. Geophys*. *Res*., **84**, 5029–5033.
800 Miyazaki, S., K. Saito. *et al*., 2015: The GRENE-TEA model intercomparison project
801 (GTMIP): Overview and experiment protocol for stage 1. *Geosci*. *Model Develop*., **8**,
802 2841–2856, https://doi.org/10.5194/gmd-8-2841-2015.
803 Nepstad, D. C., C. R. de Carvalho, E. A. Davidson, P. H. Jlpp, P. A. Lefebvre, G. H.
804 Negrelros, E. D. da Silva, T. A. Stone, S. E. Trumbore, and S. Vielra, 1994: The role of
805 deep roots in the hydrological and carbon cycles of Amazonian forests and pastures.
806 *Nature*, **372**, 666–669.
807 Ohta, T., A. Kotani, Y. Iijima, T. C. Maximov, S. Ito, M. Hanamura, A. V. Kononov,
808 and A. P. Maximov, 2014: Effects of waterlogging on water and carbon dioxide fluxes

809 and environmental variables in a Siberian larch forest, 1998–2011. *Agric*. *For*.
810 *Meteorol*., **188**, 64–75, https://doi.org/10.1016/j.agrformet.2013.12.012.
811 Oleson, K. W., D. M. Lawrence, G. B. Bonan, M. G. Flanner, E. Kluzek, P. J.
812 Lawrence, et al., 2010: Technical description of version 4.0 of thecommunity land
813 model (CLM). NCAR technical note, NCAR/TN-478+STR, pp 257.
814 Park, H., T. Yamazaki, K. Yamamoto, and T. Ohta, 2008: Tempo-spatial characteristics
815 of energy budget and evapotranspiration in the eastern Siberia. *Agric*. *For*. *Meteorol*.,
816 **148**, 1990–2005, https://doi.org/10.1016/j.agrformet.2008.06.018.
817 Park, H., Y. Iijima, H. Yabuki, T. Ohta, J. Walsh, Y. Kodama, and T. Ohata, 2011: The
818 application of a coupled hydrological and biogeochemical model (CHANGE) for
819 modeling of energy, water, and CO2 exchanges over a larch forest in eastern Siberia. *J*.
820 *Geophys*. *Res*., **116**, D15102, doi:10.1029/2010JD015386.
821 Park, H., A N. Fedorov, M. N. Zheleznyak, P. Y. Konstantinov, and J. E. Walsh, Effect
822 of snow cover on pan-Arctic permafrost thermal regimes. *Clim*. *Dyn*., **44**, 2873–2895.
823 Park, H., Y. Kim, and J. S. Kimball, 2016: Widespread permafrost vunerability and soil
824 active layer increases over the high northern latitudes inferred from satellite remote
825 sensing and process model assessments. *Remote Sens*. *Environ*., **175**, 349–358,
826 https://doi.org/10.1016/j.rse.2015.12.046.
827 Park, H., S. Launiainen, P. Y. Konstantinov, Y. Iijima, and A. N. Fedorov, 2018:
828 Modeling the effect of moss cover on soil temperature and carbon fluxes at a tundra site
829 in Northeastern Siberia. *J*. *Geophys*. *Res*.-*Biogeosci*., **123**,
830 https://doi.org/10.1029/2018JG004491.
831 Risi, C., and Coauthors, 2016: The water isotopic version of the land-surface model
832 ORCHIDEE: Implementation, evaluation, sensitivity to hydrological parameters.
833 *Hydrol*. *Curr*. *Res*., **7**, 258, doi: 10.4172/2157-7587.1000258.
834 Serreze, M. C., D. H. Bromwich, M. P. Clark, A. J. Etringer, T. Zhang, and R.
835 Lammers, 2002: Large-scale hydro-climatology of the terrestrial Arctic drainage
836 system. *J*. *Geophys*. *Res*., **107**, 8160, https://doi.org/10.1029/2001JD000919.
837 Sturm, C., Q. Zhang, and D. Noone, 2010: An introduction to stable water isotopes in
838 climate models: Benefits of forward proxy modelling for paleoclimatology. *Climate*
839 *Past*, **6**, 115–129, https://doi.org/10.5194/cp-6-115-2010.
840 Sugimoto, A., D. Naito, N. Yanagisawa, K. Ichiyanagi, N. Kurita, J. Kubota, T. Kotake,
841 T. Ohata, T. C. Maximov, and A. N. Fedorov, 2003: Characteristics of soil moisture in
842 permafrost observed in East Siberian taiga with stable isotopes of water. *Hydrol*.
843 *Process*., **17**, 1073–1092, https://doi.org/10.1002/hyp.1180.

844 Tan, A., J. C. Adam, and D. P. Lattenmaier, 2011: Change in spring snowmelt timing in
845 Eurasian Arctic rivers. J. Geophys. Res., 116, D3,
846 https://doi.org/10.1029/2010JD014337.
847 Ueta, A., A. Sugimoto, Y. Iijima, H. Yabuki, T. C. Maximov, T. A. Velivetskaya, and
848 A. V. Ignatiev, 2013: Factors controlling diurnal variation in the isotopic composition
849 of atmospheric water vapour observed in the taiga, eastern Siberia. *Hydrol*. *Proc*., **27**,
850 2295–2305, doi:10.1002/hyp.9361.
851 Vasil'chuk, Y. K., V. Shevchenko, A. Lisitzin, N. Budantseva, S. Vorobiov, S. Kirpotin
852 et al., 2016: Oxygen isotope and deuterium composition of snow cover on the profile of
853 Western Siberia from Tomsk to the Gulf of Ob. *Dokl*. *Earth Sc*., **471**, 1284–1287,
854 doi:10.1134/S1028334X1612014X.
855 Welp, L., J. Randerson, J. Finlay, S. Davydov, G. Zimova, A. Davydova, et al., 2005: A
856 high-resolution time series of oxygen isotopes from the Kolyma River: implications for
857 the seasonal dynamics of discharge and basin-scale water use. *Geophys*. *Res*. *Lett*., **32**,
858 L14401, https://doi.org/10.1029/2005GL022857.
859 White, M. A., P. E. Thornton, and S. W. Running, 1997: A continental phenology
860 model for monitoring vegetation responses to interannualclimatic variability. *Global*
861 *Biogeochem*. *Cycles*, **11**, 217–234. https://doi.org/10.1029/97GB00330.
862 Williams, M., B. E. Law, P. M. Anthoni, and M. Unsworth, 2001: Using a simulation
863 model and ecosystem flux data to examine carbon-water interactions in ponderosa pine.
864 *Tree Physiol*., **21**, 287–298.
865 Woo, M., D. L. Kane, S. K. Carey, and D. Yang, 2008: Progress in permafrost
866 hydrology in the new millennium. *Permafrost Periglac*. *Process*., **19**, 237–254.
867 Yang, D., B. Ye, and A. Shiklomanov, 2004: Discharge characteristics and changes
868 over the Ob river watershed in Siberia. *J*. *Hydrometeorol*., **5**, 595–610.
869 Yang, Y., R. J. Donohue, and T. R. McVicar. 2016. Global estimation of effective plant
870 rooting depth: Implications for hydrological modeling, Water Resour. Res., 52, 8260–
871 8276, doi:10.1002/2016WR019392
872 Ye, H., S. Ladochy, D. Yang, T. Zhang, X. Zhang, and M. Ellison, 2004: The impact of
873 climatic conditions on seasonal river discharges in Siberia. *J*. *Hydrometeorol*., **5**, 286–
874 295.
875 Yoshimura, K., S. Miyazaki, S. Kanae, and T. Oki, 2006. Iso-MATSIRO, a land surface
876 model that incorporates stable water isotopes. *Global Planet*. *Change*, **51**, 90–107,
877 https://doi.org/10.1016/j.gloplacha.2005.12.007.

Yoshimura, K., M. Kanamitsu, D. Noone, and T. Oki, 2008: Historical isotope simulation using Reanalysis atmospheric data. *J. Geophys. Res.*, **113**, D19108, doi:10.1029/2008JD010074.

Zhang, K., J. S. Kimball, Q. Mu, L. A. Jones, S. J. Goetz, and S. W. Running, 2010: Satellite based analysis of northern ET trends and associated changes in the regional water balance from 1983 to 2005. J. Hydrol., 379, 92–110, https://doi.org/10.1016/j.jhydrol.2009.09.047.

Table 1. Summary of the separation of snowmelt and rainfall contributions to evapotranspiration and the subcomponents (mm yr^{-1}) in the three experiments, averaged for the study period (1980–2016). Numbers in parentheses represent individual percentages to the total of either evapotranspiration or the subcomponents.

Exp	*ET*			E_t			E_i			E_s		
	total	snow	rain	total	snow	rain	total	snow	rain	total	snow	rain
S_{CN}	185.7	37.0 (19.9)	148.7 (80.1)	117.2	16.6 (14.2)	100.6 (85.8)	33.1	13.3 (40.2)	19.8 (59.8)	35.5	7.1 (20.0)	28.4 (80.0)
S_{MT}	189.4	37.6 (19.9)	151.8 (80.1)	120.7	17.3 (14.3)	103.4 (85.7)	33.0	13.2 (40.0)	19.8 (60.0)	35.7	7.1 (19.9)	28.6 (80.1)
S_{AB}	185.9	37.0 (19.9)	148.9 (80.1)	117.3	16.7 (14.29	100.6 (85.8)	33.1	13.3 (40.2)	19.8 (59.8)	35.5	7.1 (20.0)	28.4 (80.0)
Mean	187.0	37.2 (19.9)	149.8 (80.1)	118.4	16.9 (14.3)	101.5 (85.7)	33.1	13.3 (40.2)	19.8 (59.8)	35.6	7.1 (19.9)	28.5 (80.1)

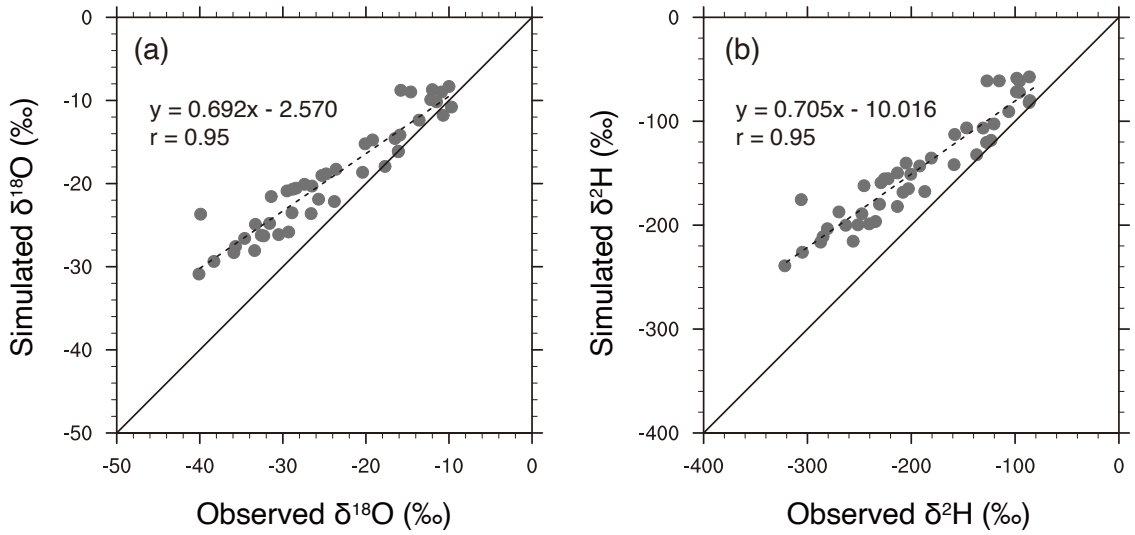

Figure 1. Comparison of IsoGSM-simulated isotope values used for CHANGE simulation to the records observed at Yakutsk station (1996–2000), archived as part of the Global Network of Isotopes in Precipitation by the International Atomic Energy Agency. Overestimated isotope values were adjusted to the observations using a scaling coefficient of 1.3.

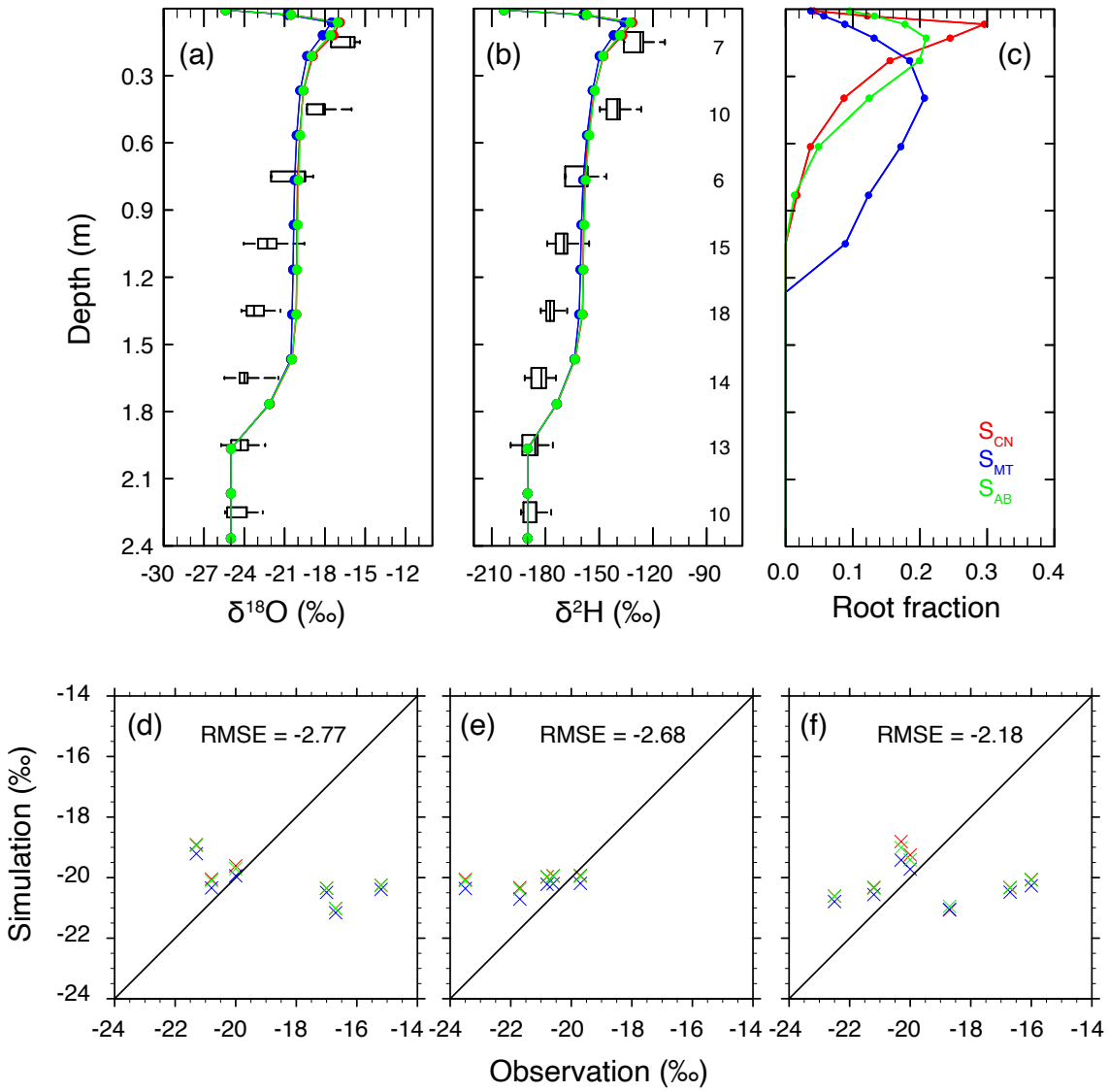

Figure 2. Comparison of (a) oxygen and (b) hydrogen simulated by the three experiments plotted against observations of analyzed soil cores sampled in March 2010. The samples within each 30-cm depth were integrally averaged, showing the distributions as boxplots. Numbers on the right in (b) refer to the sample numbers used for the average. The vertical root profiles of the three experiments are compared in (c). The model-averaged oxygen isotopic ratios of two soil layers, that is, (d) 0–0.3 m and (e) 0.3–0.6 m, and (f) transpiration are compared against the values sampled during the growing seasons of 1998–2000 at the same study site (Sugimoto et al., 2003). Modeled isotope ratios were averaged for 10 days prior to the observation date.

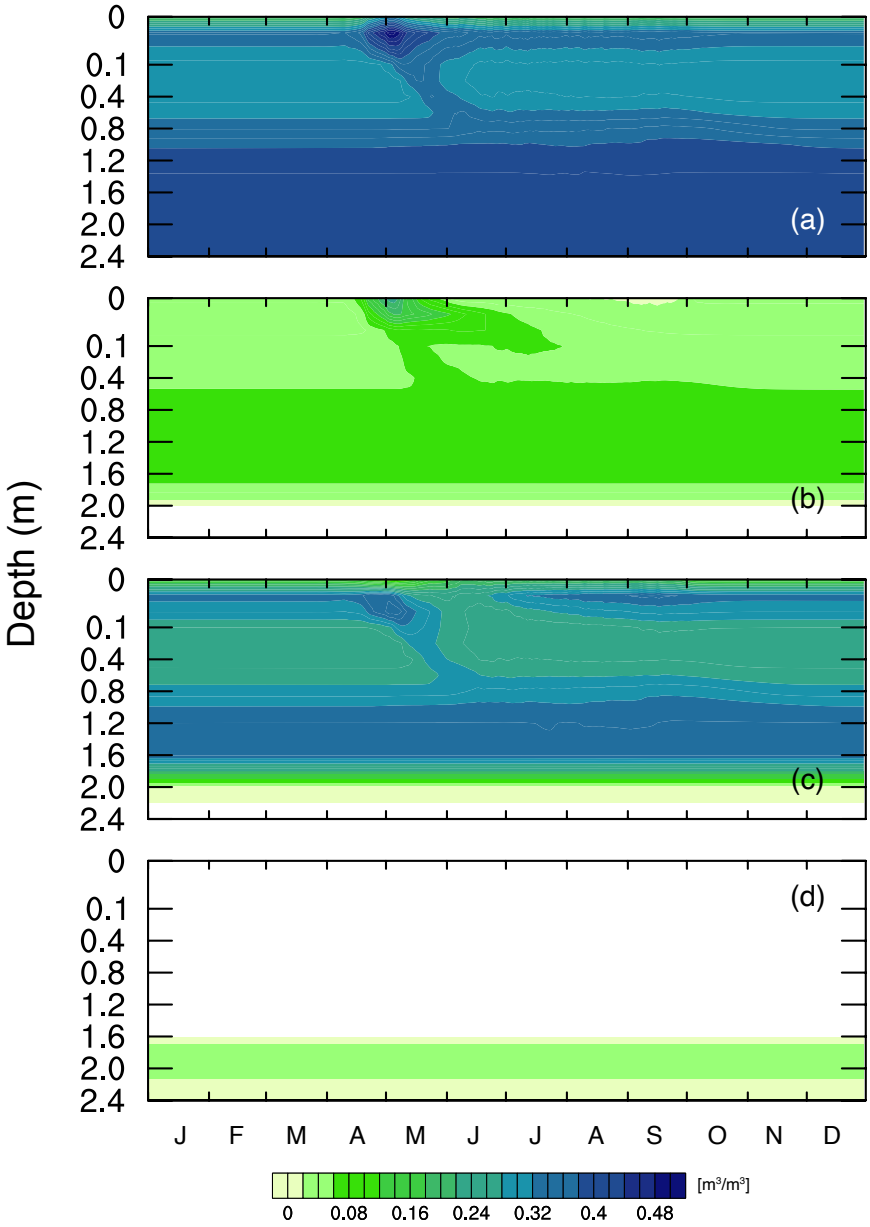

Figure 3. Seasonal variability of the vertical profile of (a) soil moisture and the separated (b) snowmelt, (c) rainfall, and (d) permafrost-originated waters, averaged for each date during 1980–2016 in the case of the control experiment.

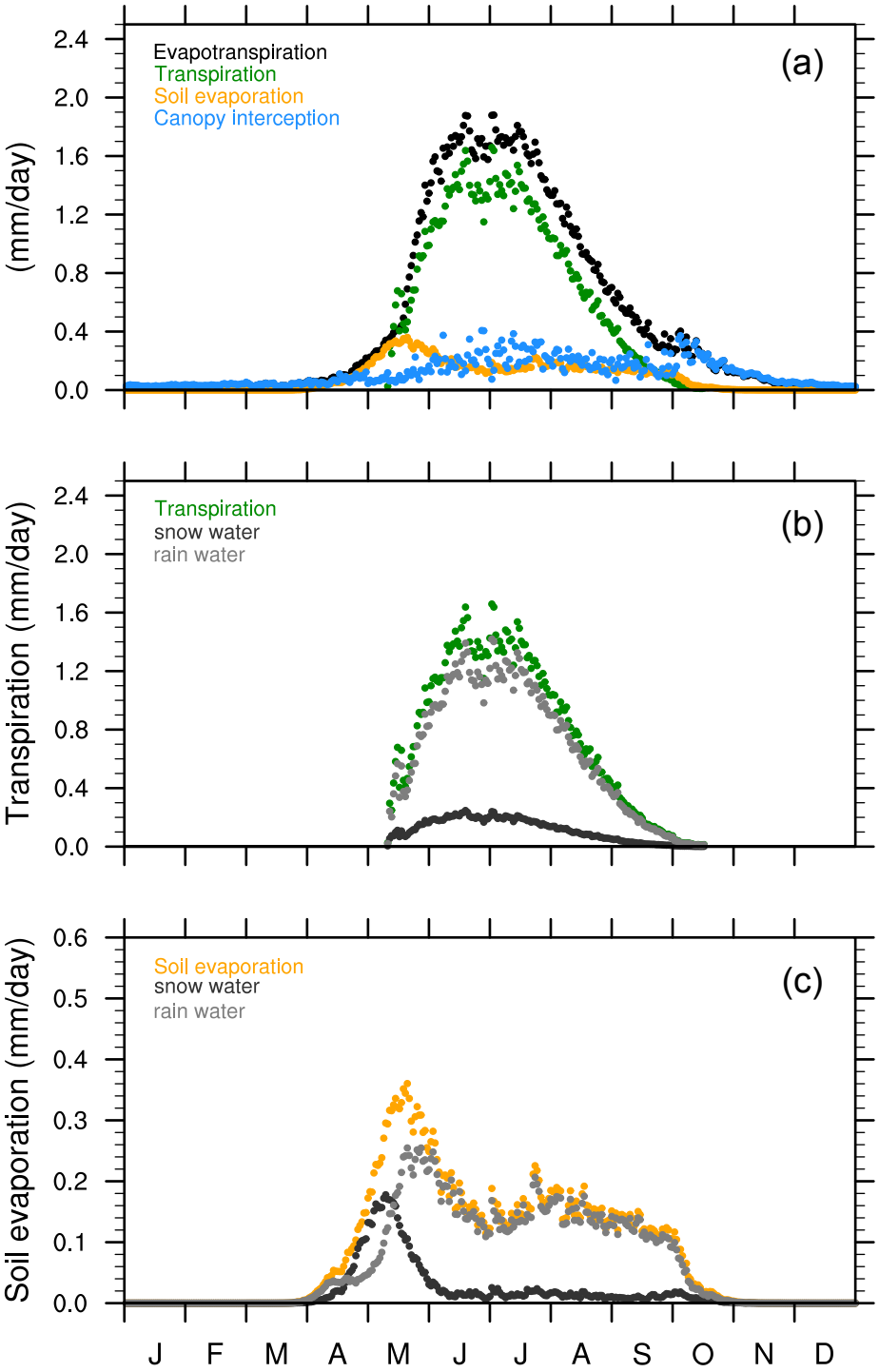

Figure 4. Time series for (a) daily evapotranspiration and the subcomponents averaged for each date during 1980–2016 in the case of the control experiment, and the variation of the contributions of snowfall and rainfall to (b) transpiration and (c) soil evaporation.

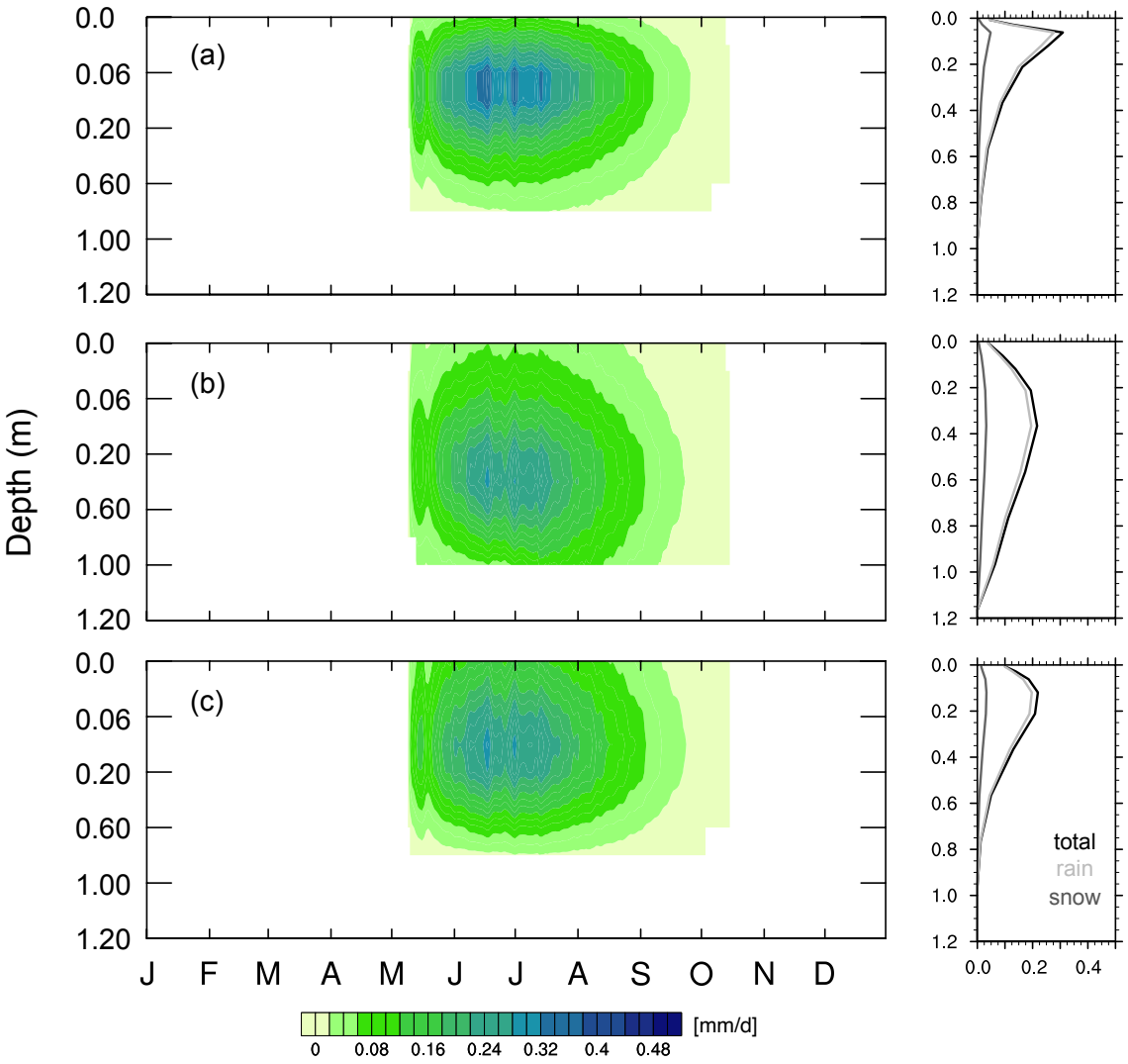

Figure 5. Seasonal variability of vertically distributed transpiration simulated by the three experiments: (a) S_{CN}, (b) S_{MT}, and (c) S_{AB}, averaged for each date during 1980–2016 (left panels), and the associated averaged vertical profiles of rainfall and snowmelt used for transpiration in the individual experiments (right-hand panels).

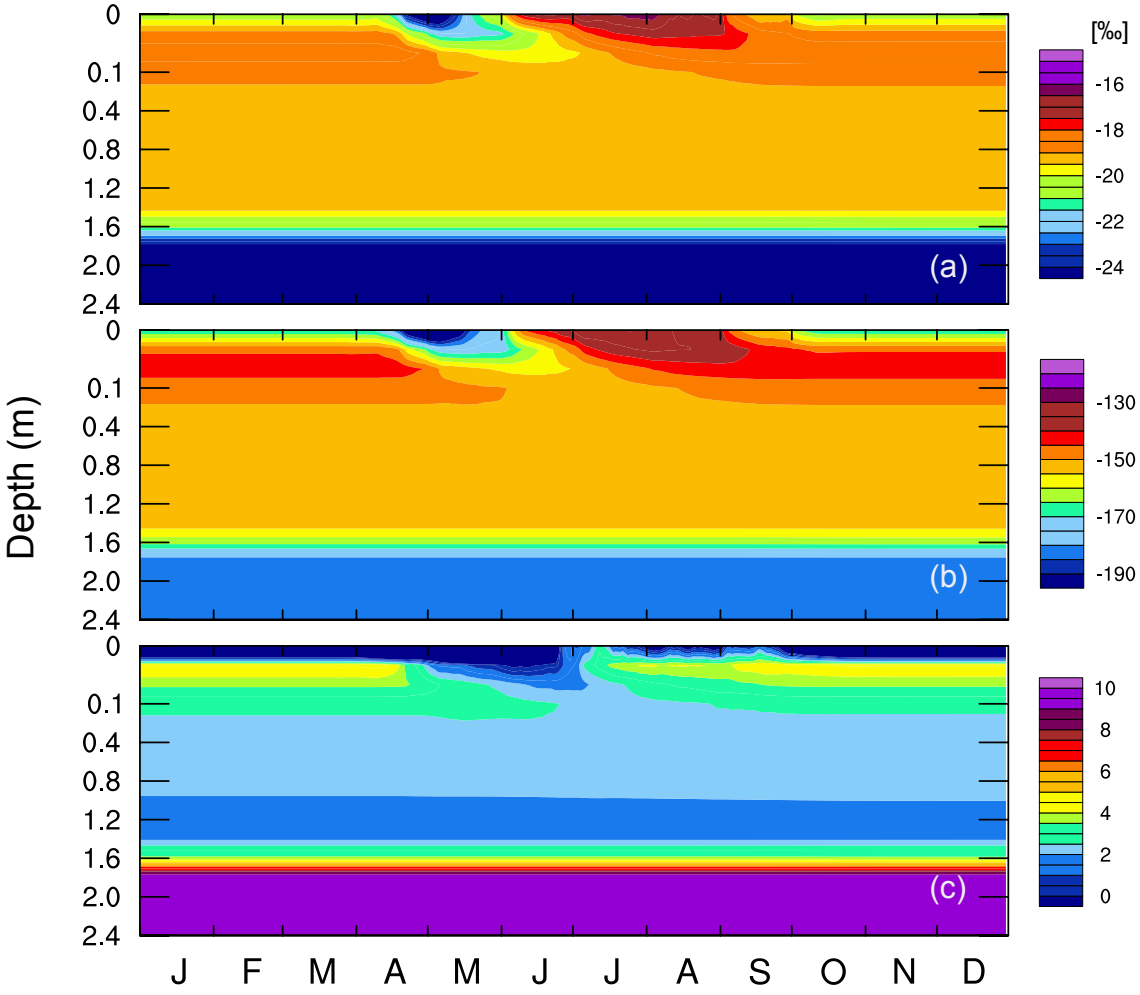

Figure 6. Seasonal variability of vertically distributed daily (a) oxygen, (b) hydrogen, and (c) d-excess isotopes, averaged for each date during 1980–2016 in the case of the control experiment.

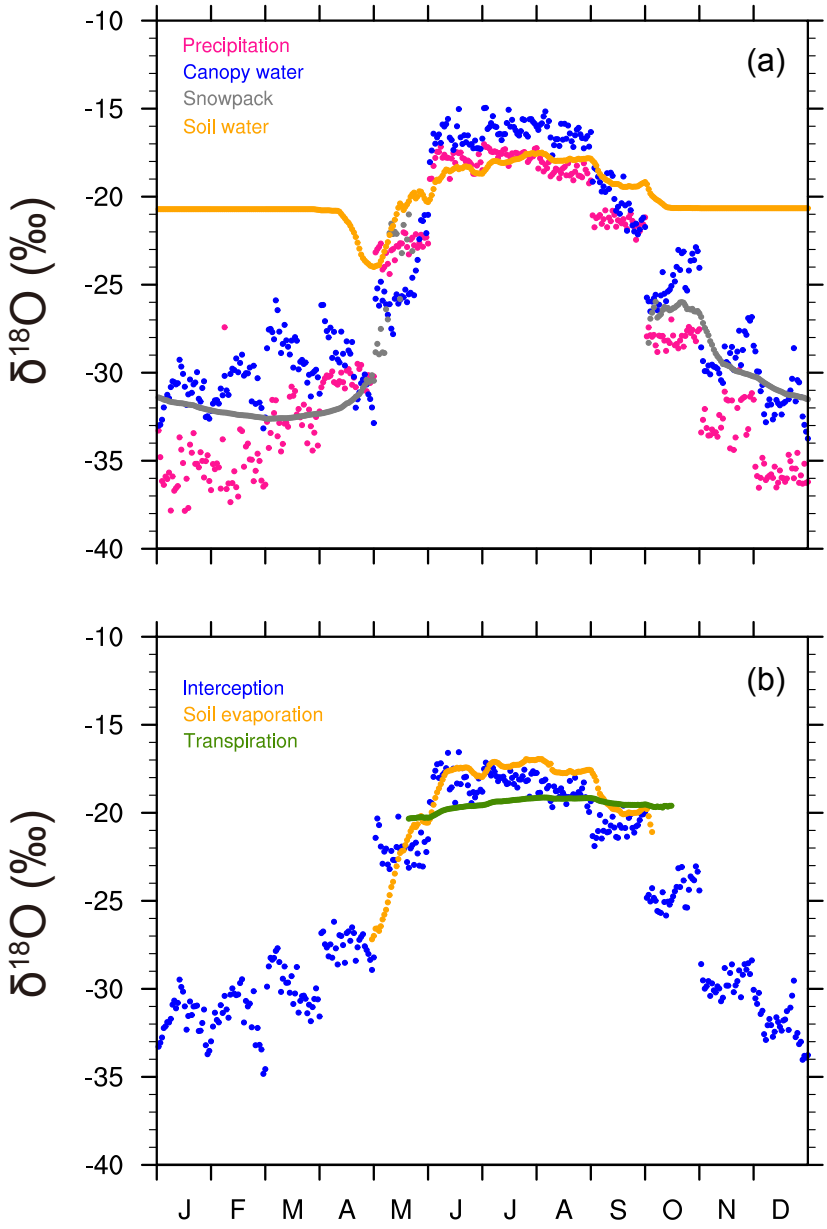

Figure 7. Time series of daily (a) oxygen isotope of precipitation-derived water storages of canopy, snow, and soil, and (b) evaporation from the surfaces and transpiration, averaged for each date during 1980–2016 in the case of the control experiment. The isotope ratio of soil water in (a) was averaged for 0–10-cm soil layers.

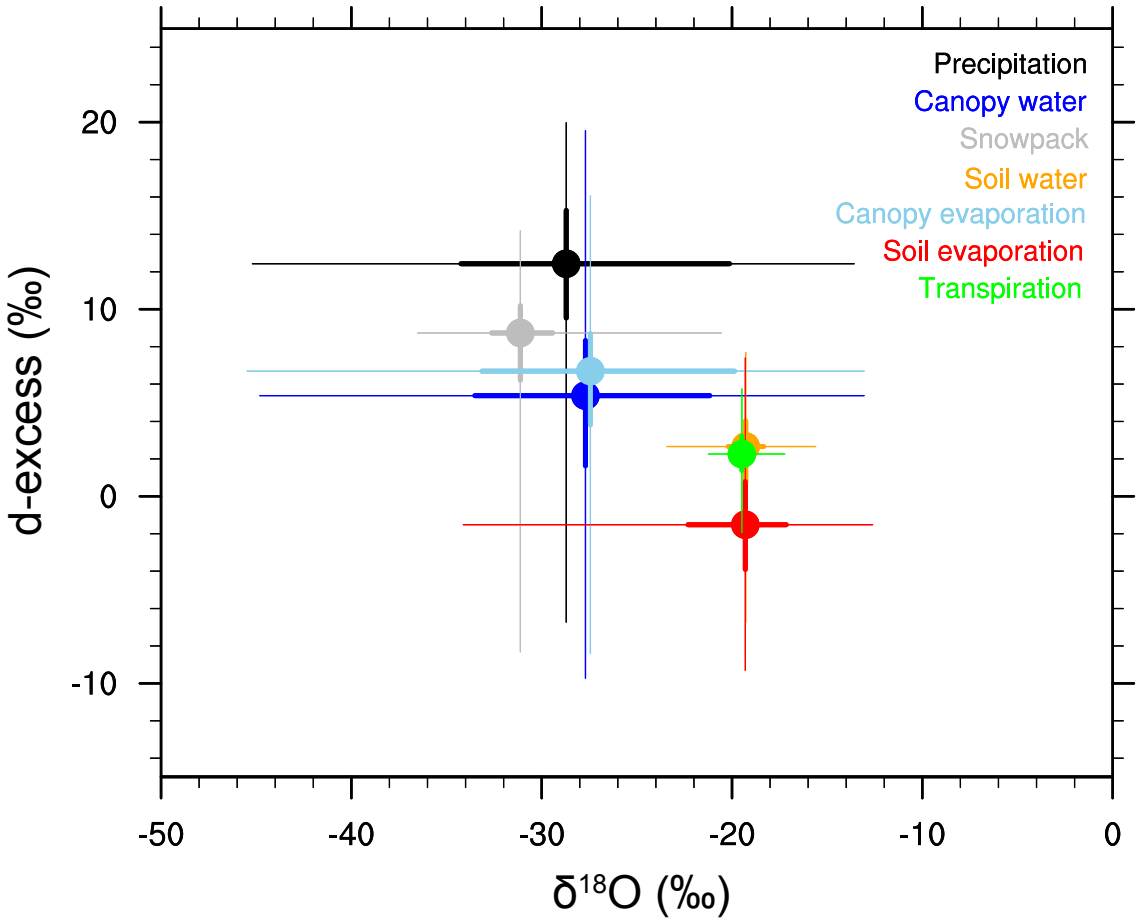

Figure 8. Isotopic plots of oxygen isotope and d-excess grouping precipitation, canopy water, snow, canopy evaporation, soil evaporation, transpiration, and soil water with different colors. The dots indicate medians of the interquartile ranges in boxplots analyzed using monthly averaged values, and the thick lines in the vertical and horizontal directions represent the ranges of the low and high quartiles in the boxplots of individual compositions. The thin lines show the maximum and minimum distribution of the monthly averaged values for the compositions.

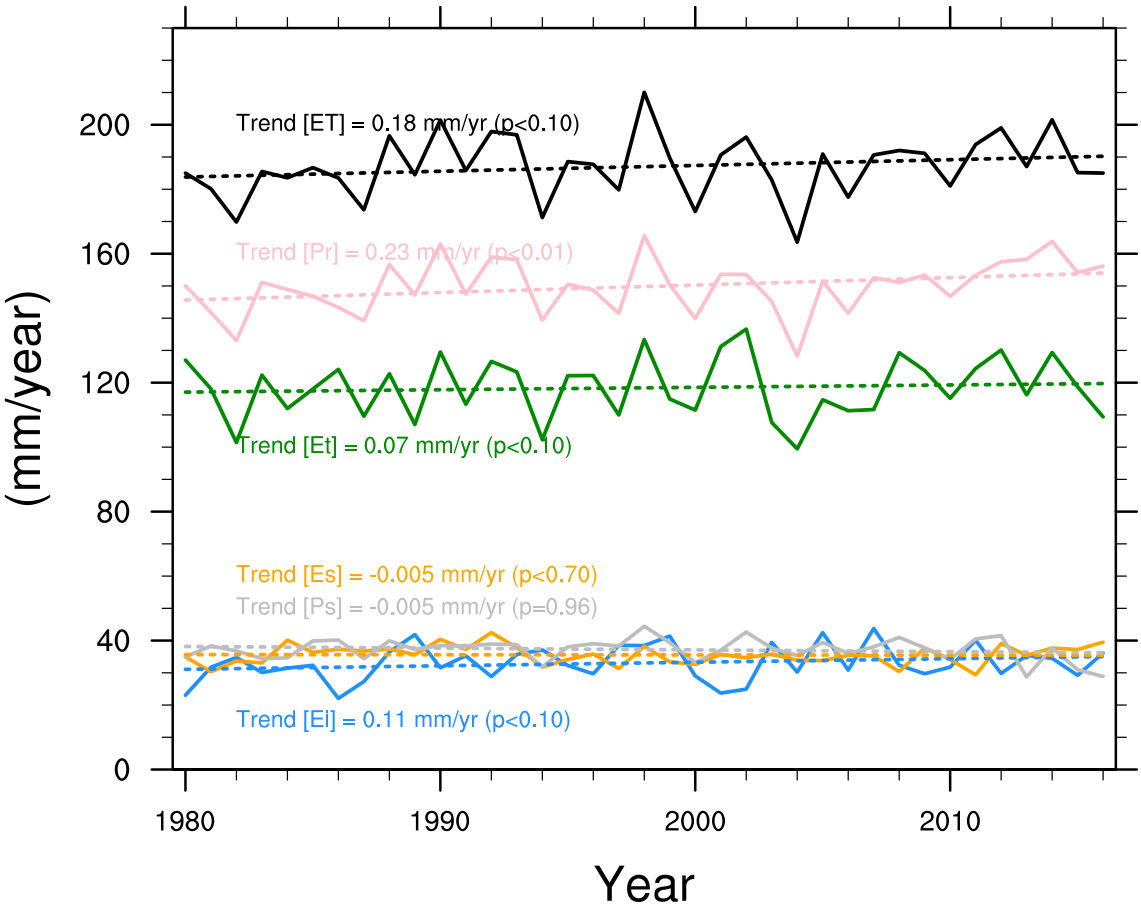

Figure 9. Interannual variability of the simulated evapotranspiration and subcomponents with rainfall (P_r) and snowmelt (P_s) waters used for evapotranspiration. The dotted lines indicate the trend of the individual variables.

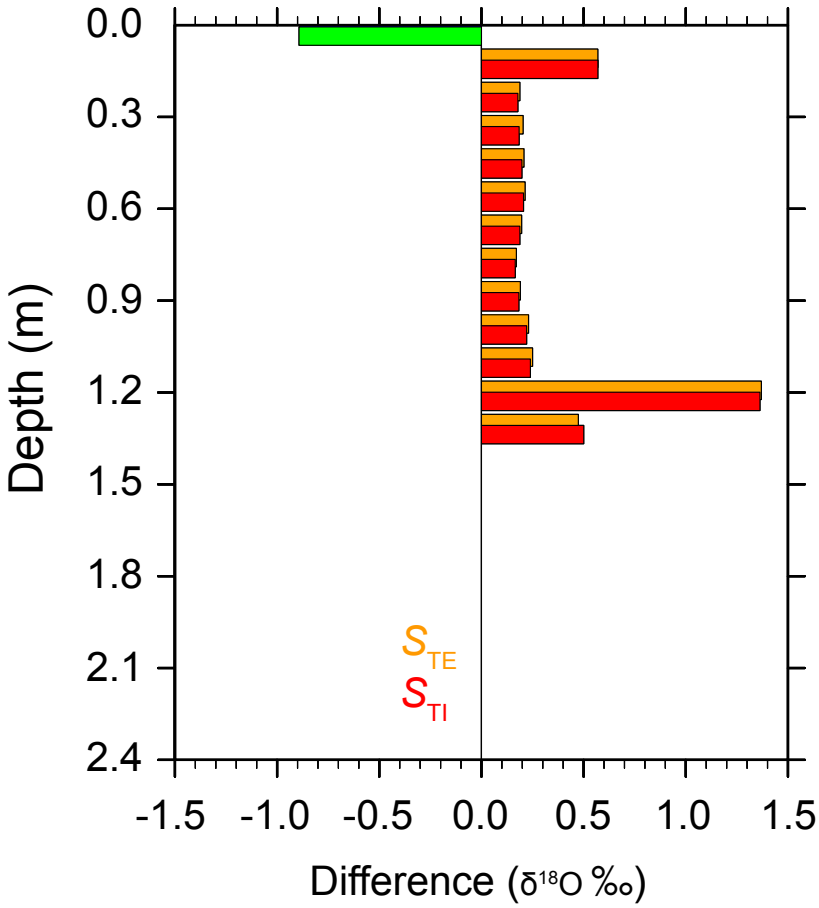

Figure 10. Vertical difference in soil water $\delta^{18}O$ between the sensitivity experiments with root depths extended to 1.56 m and the control experiment in March 2010, when the observational records were used for validation of the simulations. The two sensitivity experiments differed in that the soil freezing stress by permafrost was excluded (S_{TE}) or included (S_{TI}).

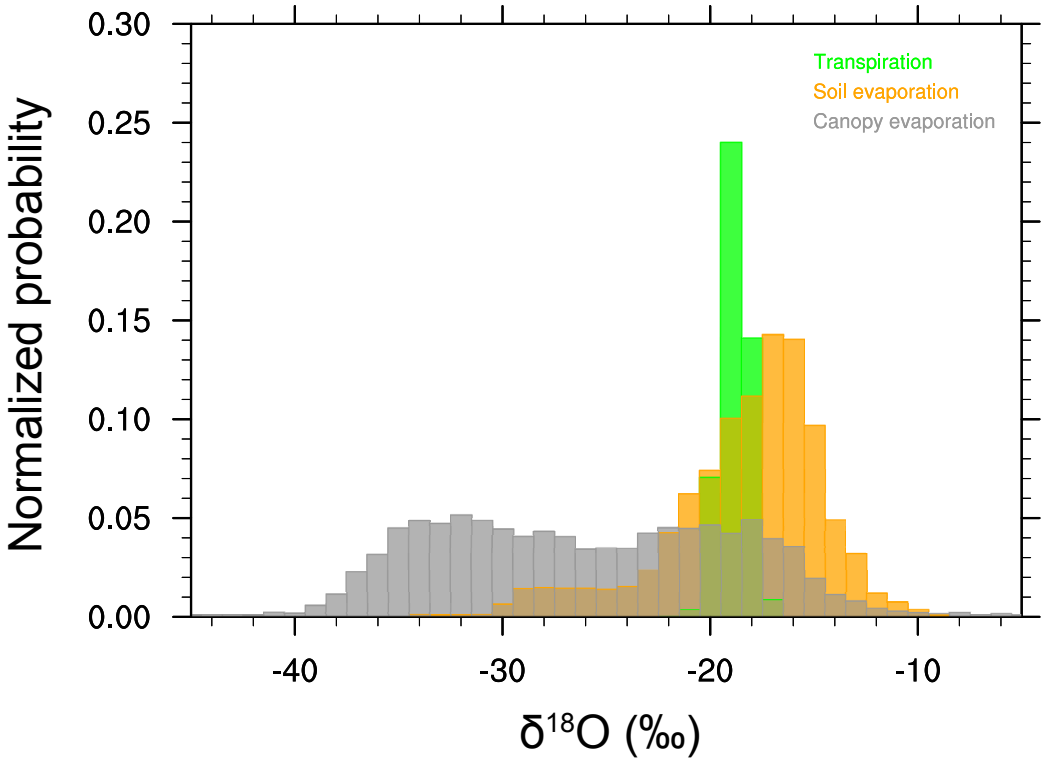

Figure 11. Normalized distribution of the $\delta^{18}O$ of *ET* components (soil and canopy evaporation and transpiration) during 1980–2016.